ACS APPLIED MATERIALS & INTERFACES

ACS AUTHORCHOICE

www.acsami.org

Research Article

$SrTiO_3/Bi_4Ti_3O_{12}$ Nanoheterostructural Platelets Synthesized by Topotactic Epitaxy as Effective Noble-Metal-Free Photocatalysts for pH-Neutral Hydrogen Evolution

Marjeta Maček Kržmanc,* Nina Daneu, Alja Čontala, Saswati Santra, Khaja Mohaideen Kamal, Blaž Likozar, and Matjaž Spreitzer

Cite This: *ACS Appl. Mater. Interfaces* 2021, 13, 370−381

Read Online

ACCESS | Metrics & More | Article Recommendations | Supporting Information

ABSTRACT: Low-temperature hydrothermal epitaxial growth and topochemical conversion (TC) reactions offer unexploited possibilities for the morphological engineering of heterostructural and non-equilibrium shape (photo)catalyst particles. The hydrothermal epitaxial growth of $SrTiO_3$ on $Bi_4Ti_3O_{12}$ platelets is studied as a new route for the formation of novel nanoheterostructural $SrTiO_3/Bi_4Ti_3O_{12}$ platelets at an intermediate stage or (100)-oriented mesocrystalline $SrTiO_3$ nanoplatelets at the completed stage of the TC reaction. The $Bi_4Ti_3O_{12}$ platelets act as a source of $Ti(OH)_6^{2-}$ species and, at the same time, as a substrate for the epitaxial growth of $SrTiO_3$. The dissolution of the $Bi_4Ti_3O_{12}$ platelets proceeds faster from the lateral direction, whereas the epitaxial growth of $SrTiO_3$ occurs on both bismuth-oxide-terminated basal surface planes of the $Bi_4Ti_3O_{12}$ platelets. In the progress of the TC reaction, the $Bi_4Ti_3O_{12}$ platelet is replaced from the lateral ends toward the interior by $SrTiO_3$, while $Bi_4Ti_3O_{12}$ is preserved in the core of the heterostructural platelet. Without any support from noble-metal doping or cocatalysts, the $SrTiO_3/Bi_4Ti_3O_{12}$ platelets show stable and 15 times higher photocatalytic H_2 production (1265 $\mu mol\cdot g^{-1}\cdot h^{-1}$; solar-to-hydrogen (STH) efficiency = 0.19%) than commercial $SrTiO_3$ nanopowders (81 $\mu mol\cdot g^{-1}\cdot h^{-1}$; STH = 0.012%) in pH-neutral water/methanol solutions. A plausible Z scheme is proposed to describe the charge-transfer mechanism during the photocatalysis.

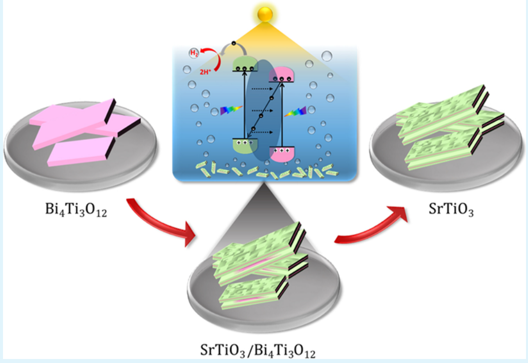

KEYWORDS: *hydrothermal epitaxial growth, topochemical conversion, perovskites, $SrTiO_3$, Aurivillius-phase layer structures, $Bi_4Ti_3O_{12}$, hydrogen evolution*

1. INTRODUCTION

Utilizing sunlight to drive chemical reactions over semiconductor photocatalysts represents a promising strategy to overcome the world's problems related to energy shortages and environmental pollution. The production of storable, green H_2 fuel from water-splitting reactions addresses these challenges.[1−6] At the moment, the process still suffers from too-low efficiencies to become economically viable. However, recent findings about the importance of heterojunctions,[3] mesocrystallinity,[6] type of exposed facets,[2] and preferential orientation[7] for improved photocatalytic performance increasingly promote an interest in the morphological engineering of functional nanostructures. In particular, the integration of two different functional materials with different band gaps and band-edge positions has attracted a great deal of scientific and technological attention.[3,8] Such heterojunction systems lead to an improvement of the photocatalytic efficiency by enhancing the photogenerated charge carriers' separation.[3] However, designing heterostructural photocatalysts in terms of achieving the target characteristics and boosted photocatalytic performance remains challenging. The same is true for the creation of single-phase photocatalyst particles with morphologies that are different from the thermodynamic equilibrium crystal shape. The engineering of the functional characteristics of the particles based on an understanding of the nucleation and growth can ensure that rational morphological design prevails over serendipity.

Topochemical conversion (TC) reactions from Aurivillius perovskite platelets ($Bi_4Ti_3O_{12}$ and $MBi_4Ti_4O_{15}$ (M = Sr, Ba)) in molten salts (NaCl/KCl) were intensively studied for the preparation of $MTiO_3$ perovskites with non-equilibrium, platelet-shape crystallites.[9−12] However, slow ionic diffusion in the solid-state lattice at much lower hydrothermal synthesis

Received: September 9, 2020
Accepted: December 9, 2020
Published: December 22, 2020

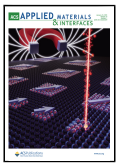

temperatures (100−200 °C) provides a better insight and understanding of the reactions at the interface compared to that in molten salt TC.[9,13] Hydrothermal TC reactions initiated by the epitaxial growth of a new phase on the precursor (template) particles enable the formation of heterostructures at an intermediate state of the transformation or after complete conversion with the formation of new-phase particles with a preserved morphology and having a crystallographic relationship with the parent phase.[13−15] In the field of hydrothermal TC reactions, Kalyani et al. performed an in-depth study of the epitaxial growth of $SrTiO_3$ on anatase (TiO_2) nanowires and their complete TC to $SrTiO_3$ mesocrystalline nanowires.[14] Exploring the TC reaction mechanisms for various template precursors will help us to engineer more complex heterostructures in the future.

In this study, we present an example of employing the TC reaction concept in the rational design of new heterostructural and mesocrystalline nanoparticles under hydrothermal conditions. We have studied the hydrothermal epitaxial growth of $SrTiO_3$ on $Bi_4Ti_3O_{12}$ template platelets with the intermediate formation of new nanoheterostructural $SrTiO_3/Bi_4Ti_3O_{12}$ platelets and after the complete transformation formation of (100)-oriented $SrTiO_3$ mesocrystalline nanoplatelets.

One of the reasons for the selection of the $SrTiO_3/Bi_4Ti_3O_{12}$ heterostructure was the interesting photocatalytic properties of the individual materials.[2,5,7,16] $SrTiO_3$ meets the thermodynamic criteria for an overall photocatalytic water-splitting reaction in terms of the appropriate band-edge positions and bandgap.[3,7,17] Several efficient H_2-evolution photocatalysts based on $SrTiO_3$ were developed using various design strategies, aiming to improve the light-harvesting capabilities and the charge-carrier separation.[2,7,18−24] For example, Zhang et al. prepared (100)-oriented $SrTiO_3$ mesocrystalline superstructural platelets by hydrothermal topotactic epitaxy from a TiO_2 mesocrystalline precursor template that consisted of assembled anatase nanocrystals with a dominant exposure of [001] facets.[7] The authors proved that these (100)-oriented $SrTiO_3$ platelets exhibited 3 times higher photocatalytic efficiency for H_2 evolution compared to conventional disordered $SrTiO_3$ systems. The abovementioned study revives the interest in further photocatalytic investigations of $SrTiO_3$ nanostructures with controlled morphologies and orientations. Similar to $SrTiO_3$, $Bi_4Ti_3O_{12}$ was also explored as a photocatalyst for H_2 generation. However, according to several reports, pure $Bi_4Ti_3O_{12}$ does not exhibit an outstanding H_2 evolution activity,[16,25] although modifications such as reduction ($Bi_4Ti_3O_{12-x}$)[16] and substitution with Cr ($Bi_4Ti_{3-x}Cr_xO_{12}$)[25−27] were confirmed to enhance considerably visible-light photocatalytic H_2 evolution from water/methanol solutions (2−4 times). For both types of modified $Bi_4Ti_3O_{12}$, the improvement was ascribed to the narrowing of the band gap and the decreased recombination of the photogenerated charges.[16,25]

The other motivation for choosing the $SrTiO_3/Bi_4Ti_3O_{12}$ system is related to the presence of similar perovskite units in both phases,[28] which promises the successful epitaxial growth of $SrTiO_3$ on $Bi_4Ti_3O_{12}$. The first attempt to prepare $Bi_4Ti_3O_{12}/SrTiO_3$ composite microplatelets was made by Zhao et al.,[29] who also used a combination of molten-salt-synthesized $Bi_4Ti_3O_{12}$ platelets and alkaline hydrothermal conditions for the growth of $SrTiO_3$. However, their $Bi_4Ti_3O_{12}$ platelets were larger (side length: 10−15 μm, 1−2 μm in this study). The major difference was in the hydrothermal step where the titanium precursor (tetrabutyl titanate) was added for the formation of $SrTiO_3$ where the titanium was not proposed to originate from the dissolution of $Bi_4Ti_3O_{12}$, as in our study. Accordingly, the reported morphology of the 10−15 μm $Bi_4Ti_3O_{12}$ platelets with sub-micrometer attachments[29] was completely different from the $SrTiO_3/Bi_4Ti_3O_{12}$ heterostructural platelets described in this study. Therefore, we believe that the presented $SrTiO_3/Bi_4Ti_3O_{12}$ composite nanostructures are unique and their functional properties are worth investigating. Our study is focused on a detailed microstructural examination of the platelets at different stages of TC in order to understand the $SrTiO_3/Bi_4Ti_3O_{12}$ interface and gain a detailed insight into the mechanism of hydrothermal epitaxial growth and the TC reaction. The epitaxial growth of $SrTiO_3$ on a layered structure of $Bi_4Ti_3O_{12}$ is expected to be more complex and illustrative than the epitaxial growth on mono metal oxides. Moreover, the anisotropic shape of the primary $Bi_4Ti_3O_{12}$ platelets with different dissolution rates of the basal and lateral surfaces is an interesting characteristic of this system that also influences the morphological evolution. The described TC mechanism provides general guidelines for the morphological engineering of nanoheterostructures through hydrothermal epitaxial growth. The study emphasizes the key parameters that must be considered for the selection of a heterostructural system, which include the structural matching at the interface, the thermodynamic stability and solubility of the involved materials, and the supersaturation. A light-induced, good, and stable H_2 production rate from a pH-neutral solution established these novel, noble-metal-free $SrTiO_3/Bi_4Ti_3O_{12}$ nanoheterostructural platelets as promising candidates in the field of photocatalytic H_2 evolution.

2. EXPERIMENTAL SECTION

2.1. Synthesis Conditions. *2.1.1. Chemicals and Materials.* All the chemicals were of analytical grade and were used as received without further purification. In the syntheses, the following reagents were involved: KCl (Sigma-Aldrich, ≥99.0%), NaCl (Merck, ≥99.7%), TiO_2 (P25, Degussa), Bi_2O_3 nanopowder (Sigma Aldrich, 99.8%), HNO_3 (VWR, 68%), $SrCl_2\cdot6H_2O$ (Sigma-Aldrich, ≥99.0%), NaOH (Fisher Chemicals, ≥98.7%). Water used for the study was purified with a system to produce ultrapure water (Purelab Option-Q7, ELGA). Commercially available $SrTiO_3$ nanopowder was used as a reference photocatalyst (Sigma-Aldrich, 20−40 nm).

2.1.2. Synthesis of $Bi_4Ti_3O_{12}$ Template Platelets. $Bi_4Ti_3O_{12}$ platelets were synthesized in molten KCl/NaCl salt using Bi_2O_3 (1.9453 g) and TiO_2 (0.5 g) nanopowders as the starting materials. To synthesize the $Bi_4Ti_3O_{12}$ platelets via the molten-salt route, the molar ratio of NaCl:KCl:Bi_2O_3:TiO_2 was optimized as 50:50:2:3. The synthesis was performed at 800 °C with a holding time of 2 h with heating and cooling rates of 10 °C/min. Details of the procedure and selected parameters are described elsewhere.[30] After the synthesis, the $Bi_4Ti_3O_{12}$ platelets were separated from the salt by washing with ultrapure water. To ensure the complete removal of any surface contamination,[12] the platelets were soaked in 2-M HNO_3 for a short time (5 min) and washed again with ultrapure water. The product particles were freeze-dried to obtain a powder with well-separated platelets.

2.1.3. Hydrothermal TC of $Bi_4Ti_3O_{12}$ to $SrTiO_3$. The TC reaction of the $Bi_4Ti_3O_{12}$ template particles to $SrTiO_3$ platelets was carried out via the hydrothermal route. $Bi_4Ti_3O_{12}$ particles were used as templates for the non-equilibrium plate-like growth of $SrTiO_3$ and as well as a source of Ti, whereas $SrCl_2\cdot6H_2O$ was the source of strontium. A large excess of $SrCl_2\cdot6H_2O$ was used to ensure supersaturation conditions and promote the nucleation of $SrTiO_3$ on both basal surface planes of the $Bi_4Ti_3O_{12}$ platelets. First, $SrCl_2\cdot6H_2O$ was

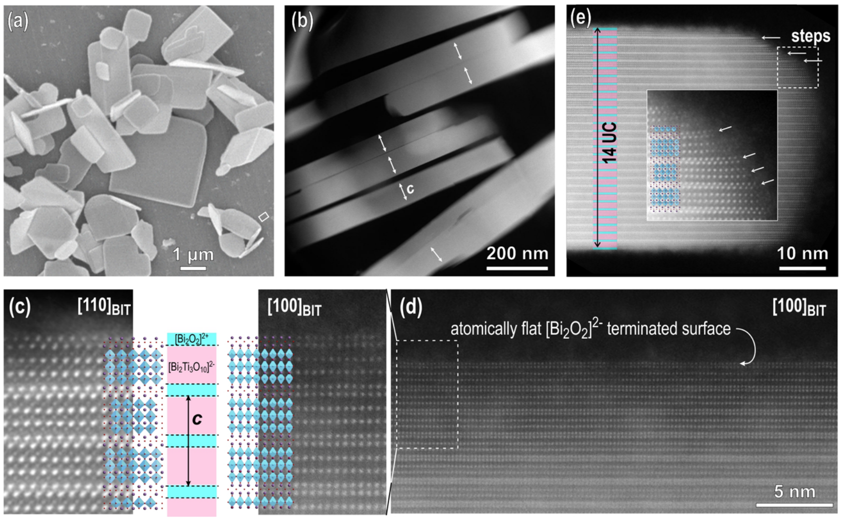

Figure 1. (a) SEM image of $Bi_4Ti_3O_{12}$ template particles. (b) Low-magnification HAADF-STEM image of edge-on-oriented $Bi_4Ti_3O_{12}$ platelets. Arrows denote the *c* axes. (c) Atomic-resolution Z-contrast images of platelets in the [100] $Bi_4Ti_3O_{12}$ and [110] $Bi_4Ti_3O_{12}$ orientations taken near the surface of the particles with overlaid structural models. The platelets are terminated by the $[Bi_2O_2]^{2+}$ layer. (d) Atomically flat (smooth) surface of the platelets as a result of layer-by-layer growth in molten salt. (e) Edge of a platelet with a thickness of 14 unit cells (UCs) (+ an additional $[Bi_2O_2]^{2+}$ layer) with steps. The magnified region shows weakly bonded adatoms on the exposed surface on the lateral side of the platelet.

dissolved in ultrapure water, and then $Bi_4Ti_3O_{12}$ platelets were admixed to the solution in an amount corresponding to the Sr:Ti molar ratio of 12:1. Suspensions were sonicated for 25 min followed by the addition of NaOH solutions. In the precursor suspension before the hydrothermal reaction, the concentrations of the $SrCl_2 \cdot 6H_2O$, $Bi_4Ti_3O_{12}$, and NaOH platelets were 0.0388, 0.00107, and 6 M, respectively. The hydrothermal syntheses were performed by stirring at 200 °C in a Berghof high-pressure reactor using a Teflon (PTFE) insert. The reaction time was varied from 1 to 15 h. After the hydrothermal synthesis, the product particles were separated from the reaction solution by centrifugation and washed several times with ultrapure water. The solid product was soaked in 1 M HNO_3 for 5 min to remove the side products, and afterward, the particles were again repeatedly washed with ultrapure water to completely remove any traces of acid. At the end, the particles were freeze-dried to obtain the final product.

2.2. Characterization of the Samples. X-ray powder diffraction was employed using a Bruker AXS D4 Endeavor with Cu Kα radiation (1.5406 Å) for the powder samples and for the platelets cast on the Si monocrystalline substrate. The weight ratio of $SrTiO_3$:$Bi_4Ti_3O_{12}$ in the heterostructural platelet was estimated from the calibration curve, which was produced from XRD measurements of the mixtures of $SrTiO_3$ and $Bi_4Ti_3O_{12}$ platelets in various weight ratios. These XRD measurements were performed for preferentially oriented platelets cast on the Si monocrystalline substrate.

A field-emission scanning electron microscope (FE-SEM, JSM 7600 F, JEOL, Japan) was used to observe the morphology of the particles. A nanoscale analysis of the platelets was performed using a 200 kV scanning transmission electron microscope (STEM, Jeol ARM 200 CF, JEOL, Japan) equipped with an energy-dispersive X-ray spectrometer (EDXS, Jeol Centurio 100). Samples of platelet-like particles for the STEM analyses were prepared using two approaches. For observations along the shorter zone axis of the platelets, the powdered sample was sonicated in absolute ethanol and a droplet of the suspension was applied to the lacey, carbon-coated copper grid. This resulted in a spontaneous alignment along the preferential orientation with the largest surface parallel to the carbon film substrate. The thickness of the platelets of up to 100 nm allowed STEM analyses without any further thinning. For edge-on observations of the platelet-like particles with a side length between 1 and 2 microns, the particles had to be thinned to electron transparency. This was accomplished by embedding the powders in epoxy resin and further mechanical and ion milling (Gatan PIPS Model 691, USA).

The Brunauer−Emmett−Teller (BET) surface areas of the powders were measured by nitrogen adsorption with a Micromeritics Gemini II 2370 nitrogen-adsorption apparatus (Norcross, GA).

Band-gap energies of the synthesized platelets were determined from their diffuse reflection spectra with $BaSO_4$ as a reference. The measurements in the ultraviolet and visible (UV−vis) spectral ranges were performed with an integrating sphere and a UV−vis spectrophotometer (Shimadzu UV-3600, Tokyo, Japan). Photoluminescence (PL) spectra of the samples were recorded using a Synergy H1 microplate reader with monochromator optics (Bio-Tek, U.S.A.) at an excitation wavelength of 320 nm.

2.2.1. Photocatalytic H_2 Evolution. The photocatalytic H_2 evolution measurements were carried out in a 50 mL quartz round-bottom flask at ambient temperature and atmospheric pressure using mixing to achieve the particle suspension. A commercial solar simulator equipped with a Xenon arc lamp (300 W, Newport) and an AM 1.5G filter was used as the light source. In a typical photocatalytic measurement, 20 mg of photocatalyst was suspended in 40 mL of aqueous solution containing 25 vol % methanol and the suspension was sonicated for 30 min to obtain a well-dispersed particle suspension. Before light irradiation, the quartz flask was sealed with a rubber septum and purged with a nitrogen flow for 40 min to remove the excess oxygen in the reaction mixture. Finally, the sealed quartz flask was placed under light irradiation. All the photocatalysts were subjected to 4 h of light irradiation, and the H_2 evolution was measured periodically every hour. The generated gas composition (1 mL) was analyzed with a gas chromatograph (GC, SRI-8610C) equipped with a thermal conductivity detector (TCD), and high-purity nitrogen was used as the carrier gas.

3. RESULTS AND DISCUSSION

The transformation of $Bi_4Ti_3O_{12}$ into $SrTiO_3$ under hydrothermal conditions is governed by the chemistry at the interface and the concentrations of the dissolved titanium and strontium species (supersaturation). In this particular TC reaction, the $Bi_4Ti_3O_{12}$ platelets act as a source of titanium and as the substrate for the epitaxial growth of $SrTiO_3$. To control and direct the growth of $SrTiO_3$ on the surface of the $Bi_4Ti_3O_{12}$ platelets, the characteristics of the latter must be studied first.

3.1. Structural Studies of $Bi_4Ti_3O_{12}$ Template Platelets.

In the first step of our investigations, we characterized the $Bi_4Ti_3O_{12}$ platelets down to the atomic scale. Knowledge about the morphology, the termination of the $Bi_4Ti_3O_{12}$ crystallites, and the nature of the surface after applying different treatment procedures following the synthesis in molten salt (and after washing with water or acid) is important for selecting the optimum strategy for the treatment of the synthesized $Bi_4Ti_3O_{12}$ powders and gives fundamental knowledge for steering and understanding the heterogeneous nucleation of $SrTiO_3$ on $Bi_4Ti_3O_{12}$ templates. Orthorhombic $Bi_4Ti_3O_{12}$ platelets grown in NaCl/KCl molten salt at 800 °C for 2 h are shown in Figure 1a. The crystallites have a typical tabular or platelet-like morphology with a side length of up to a few microns and a thickness of well below a micron.[30] The platelet-like morphology represents the equilibrium shape of $Bi_4Ti_3O_{12}$ reflecting its layered crystal structure. High-angle annular dark field (HAADF)−STEM analysis of the $Bi_4Ti_3O_{12}$ platelets after the removal of the residual salt by soaking in water and additionally in 2 M HNO_3 for a short time is shown in Figure 1b−e. A low-magnification image of edge-on-oriented $Bi_4Ti_3O_{12}$ platelets (Figure 1b) shows that most of the crystallites have a thickness below 100 nm (1 unit cell = 3.2882 nm; PDF: 01-084-6889). The morphology of the $Bi_4Ti_3O_{12}$ platelets indicates a significantly faster growth in the direction of the layers and a slower thickening perpendicular to the layers, typical for minerals with a layered structure.

Atomic-resolution STEM was used to investigate the termination of the platelets. Figure 1c shows HAADF-STEM images of $Bi_4Ti_3O_{12}$ platelets oriented along the [100] $Bi_4Ti_3O_{12}$ and [110] $Bi_4Ti_3O_{12}$ zone axes. The experimental images are overlaid with an atomic model of $Bi_4Ti_3O_{12}$ (PDF: 01-084-6889) showing the layered structure composed of $[Bi_2O_2]^{2+}$ sheets and pseudo-perovskite $[Bi_2Ti_3O_{10}]^{2-}$ blocks. Both images were recorded near the surface of the platelets and reveal that the crystallites are terminated by $[Bi_2O_2]^{2+}$ sheets. Several crystallites were examined and the analyses confirmed that all the $Bi_4Ti_3O_{12}$ platelets have this termination on both basal-plane surfaces. Observations of the crystallites at lower magnifications also showed that the basal-plane surface of the $Bi_4Ti_3O_{12}$ platelets is atomically flat on a large scale (Figure 1d), perhaps even across the whole crystallite since the presence of steps and terraces on the basal surface were never observed in the TEM. In contrast to the basal-plane surfaces, the lateral surfaces of the crystallites contain growth steps where the TiO_6 octahedra are exposed (Figure 1e). HAADF-STEM images recorded at the edge of the crystallite also imply weaker bonding of the adatoms on the exposed surface of the lateral side of the platelet (see the inset in Figure 1e). These basic differences between the basal and lateral surfaces reflect the layer-by-layer growth mode and probably influence the $Bi_4Ti_3O_{12}$ dissolution rates in different crystallographic orientations. It is expected that the dissolution of the $Bi_4Ti_3O_{12}$ platelets will proceed faster from the lateral stepped surface.[31] The $[Bi_2O_2]^{2+}$-terminated $Bi_4Ti_3O_{12}$ platelets with atomically flat basal-plane surfaces are an ideal substrate for the epitaxial growth of the perovskite $SrTiO_3$ phase due to the good match of the two phases in the $[001]Bi_4Ti_3O_{12}\|[100]SrTiO_3$ and $\{110\}Bi_4Ti_3O_{12}\|\{100\}SrTiO_3$ orientational relationship. The lattice spacings of $\{110\}Bi_4Ti_3O_{12}$ and $\{100\}SrTiO_3$ are 0.3842 and 0.3905 nm, meaning that the structural match of both phases is good, a prerequisite for successful epitaxial growth.

3.2. Background for the Selection of the TC Synthesis Conditions.

The TC reaction of the $Bi_4Ti_3O_{12}$ platelets to $SrTiO_3$ particles with a preserved, plate-like morphology under hydrothermal conditions is expected to proceed by the dissolution of $Bi_4Ti_3O_{12}$ and the concurrent precipitation of $SrTiO_3$ on the surface of the $Bi_4Ti_3O_{12}$ platelets with the only source of titanium ions being the dissolving $Bi_4Ti_3O_{12}$ crystals, whereas the concentration of Sr^{2+} ions is controlled based on the amount of strontium salt ($SrCl_2{\cdot}6H_2O$).

The lack of relevant thermodynamic data for $Bi_4Ti_3O_{12}$ limits the theoretical predictions for its dissolution and for the formation of equilibrium compounds ($SrTiO_3$, Bi_2O_3, and $Bi_{12}TiO_{20}$) as a function of the physicochemical conditions (pH, synthesis temperature (T), and concentrations of ions). Hence, the first approximate experimental conditions for the formation of $SrTiO_3$ from $Bi_4Ti_3O_{12}$ were established based on the reported thermodynamic modeling for the crystallization of $SrTiO_3$ from TiO_2 under hydrothermal conditions and previous empirical studies of $SrTiO_3$ growth on different titanate precursors.[13−15,32] Lencka and Riman[32] calculated a phase-stability diagram for the Sr−Ti hydrothermal system of anatase and hydrous TiO_2 gel. Later, Kalyani et al.[13] extended the diagram to rutile. Their results show that the formation of $SrTiO_3$ from titanate precursors requires a basic pH, where the $Ti(OH)_6{}^{2-}$ ions are the predominant aqueous titanium species.[13−15,32,33] Considering that $Sr(OH)_2$ exhibits a high solubility in aqueous media at higher temperatures of $100\ °C \le T \le 300\ °C$, the formation of $SrTiO_3$ under hydrothermal conditions is presented using the following equation:[13,15]

$$Ti(OH)_6{}^{2-}(aq) + Sr^{2+}(aq) \rightarrow SrTiO_3(s) + 3H_2O \qquad (1)$$

In our system, under alkaline conditions, the Sr^{2+} ions from the dissolved $SrCl_2$ precipitate first as $Sr(OH)_2$, which then dissolves at higher temperatures ($100\ °C \le T \le 200\ °C$). The $Ti(OH)_6{}^{2-}$ species form presumably by the dissolution of $Bi_4Ti_3O_{12}$ in alkaline media according to eq 2.

$$\begin{aligned} &Bi_4Ti_3O_{12} + 12H_2O + 6OH^- \\ &\quad \Rightarrow 4Bi(OH)_3 + 3Ti(OH)_6{}^{2-} \end{aligned} \qquad (2)$$

It is expected that the precipitation of the $SrTiO_3$ on $Bi_4Ti_3O_{12}$ platelets (heterogeneous nucleation) also proceeds following eq 1. According to the theory of heterogeneous nucleation, the energy for the formation of a critical nucleus is proportional to the third power of the interfacial free energy and inversely proportional to the square of the supersaturation.[34] In other words, the energy barrier for the nucleation of $SrTiO_3$ on $Bi_4Ti_3O_{12}$ is lowered by the close structural match between the $Bi_4Ti_3O_{12}$ substrate and the precipitating $SrTiO_3$ phase and by the higher concentrations of $Ti(OH)_6{}^{2-}$ and Sr^{2+} ions (supersaturation). Taking into account the orientation relationship of $[001]Bi_4Ti_3O_{12}\|[100]$-$SrTiO_3$ and $\{110\}Bi_4Ti_3O_{12}\|\{100\}SrTiO_3$, the theoretical lattice match between $Bi_4Ti_3O_{12}$ and $SrTiO_3$ is good. The supersaturation (eq 3) in our system is defined as the ratio between the product of the activities of aqueous species immediately before the $SrTiO_3$ formation and the solubility product K_s, which is the reciprocal of the equilibrium constant of eq 1:[13]

$$S = \frac{a(Ti(OH)_6{}^{2-})a(Sr^{2+})}{K_s} \qquad (3)$$

In our reaction system, the concentration of $Ti(OH)_6^{2-}$ is a complex function of $Bi_4Ti_3O_{12}$ dissolution and $SrTiO_3$ precipitation. Therefore, possibilities for the direct control of the supersaturation in terms of $Ti(OH)_6^2$ are limited. In contrast, tailoring of the supersaturation with respect to the Sr^{2+} ions is easily feasible with the initial amount of strontium salt. To ensure the supersaturation conditions for $SrTiO_3$ formation, the selected strontium concentration with respect to the whole titanium content was higher than that required by the $SrTiO_3$ stoichiometry. The optimal concentration of $Bi_4Ti_3O_{12}$ was determined during our preliminary experiments to be 0.00107 M.[30] This relatively low concentration was also selected to avoid the eventual precipitation of bismuth titanium compounds (e.g., $Bi_{12}TiO_{20}$) that would compete with $SrTiO_3$ for the $Ti(OH)_6^{2-}$ species.

Before studying the $Bi_4Ti_3O_{12}$-to-$SrTiO_3$ transformation, the stability of the initial $Bi_4Ti_3O_{12}$ template platelets at 200 °C and in highly alkaline conditions (6 M NaOH) without the presence of Sr^{2+} ions was verified. The solubility and dissolution rates of the $Bi_4Ti_3O_{12}$ platelets in the alkaline media should be moderate to prevent their complete dissolution and the disintegration of the substrate for epitaxial growth, as was observed in some other systems.[35,36] A qualitative evaluation of the stability of the $Bi_4Ti_3O_{12}$ platelets under applied alkaline hydrothermal conditions (6 M NaOH, 200 °C/15 h) in the absence of $SrCl_2$ revealed no significant change in the platelet's average side length, while the general platelet-like morphology was well preserved in spite of the harsh conditions. The major difference was observed on the lateral surfaces where the beginning of the exfoliation was observed. This is a result of the limited incongruent dissolution of $[Bi_2O_2]^{2+}$ sheets and the pseudo-perovskite $[Bi_2Ti_3O_{10}]^{2-}$ blocks from the lateral direction (Figure S1, Supporting Information). Considering the low concentration of $Bi_4Ti_3O_{12}$ platelets (0.00107 M), their solubility in 6 M NaOH is relatively low. Nevertheless, under similar hydrothermal conditions in the presence of dissolved Sr^{2+} ions, it is assumed that $SrTiO_3$ formation according to eq 1 is the driving force for $Bi_4Ti_3O_{12}$ dissolution. The transformation of the initial $Bi_4Ti_3O_{12}$ template particles to the $SrTiO_3$ platelets was studied for a system with a strontium content that is 12 times higher than required by the $SrTiO_3$ stoichiometry. The strontium concentration (0.0388 M) was 4 times larger than in our previous study.[30] With a higher supersaturation, we aim to decrease the energy barrier for the nucleation of $SrTiO_3$ and promote its growth over the whole basal-plane surfaces of $Bi_4Ti_3O_{12}$ platelets and consequently ensure that the $SrTiO_3/Bi_4Ti_3O_{12}$ heterostructural and final $SrTiO_3$ particles maintain the platelet-like shape of the initial template.[13,34]

3.3. Mechanistic Interpretation of the $Bi_4Ti_3O_{12}$-to-$SrTiO_3$ TC Process.

The progress of the hydrothermal TC reaction was first inspected by XRD. Figure 2 and Figure S2 (Supporting Information) show the XRD patterns of the acid-washed platelets (free of side products) after different reaction times. The XRD patterns of the initial $Bi_4Ti_3O_{12}$ platelets with a high (001) preferential orientation are also shown in Figure 2 and Figure S2 for comparison. The formation of the $SrTiO_3$ was already observed after 1 h of the hydrothermal reaction (6 M NaOH, Sr/Ti = 12). The amount of $SrTiO_3$ compared to $Bi_4Ti_3O_{12}$ increased with a prolongation of the reaction time. Only $SrTiO_3$ with a (100) preferential orientation and no $Bi_4Ti_3O_{12}$ were detected after 15 h (Figure 2 and Figure S2). In the figures, $SrTiO_3$ and $Bi_4Ti_3O_{12}$ are labeled as STO and BIT, respectively.

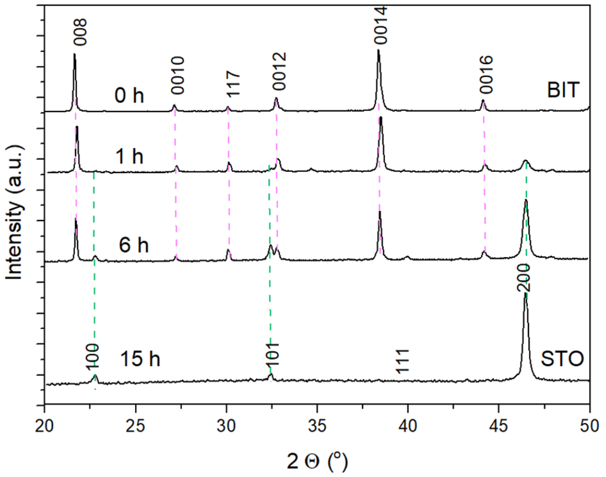

Figure 2. XRD patterns of the HNO_3-washed platelets (cast on Si monocrystalline substrate) after different times of the TC reaction (200 °C, 6 M NaOH, Sr/Ti = 12).

The side-products can carry valuable information about the TC mechanism. An insight into all the reactions accompanying the TC of $Bi_4Ti_3O_{12}$ to $SrTiO_3$ was obtained with an XRD analysis of the whole reaction product (Figure S3, Supporting Information). The results revealed the formation of $SrTiO_3$, $SrCO_3$, and Bi_2O_3. $SrCO_3$ formed through a reaction of $Sr(OH)_2$ with carbonate impurities in the NaOH chemical and with atmospheric CO_2. The formation of $SrCO_3$ also continued after the completed reaction and the opening of the autoclave when the alkaline suspension with excessive and unreacted $Sr(OH)_2$ is exposed to the atmosphere for a longer time. The formation of bismuth oxide, on the other hand, is a result of condensation of bismuth hydroxide $Bi(OH)_3$,[37] which forms during the $Bi_4Ti_3O_{12}$ dissolution. No bismuth titanium compounds (e.g., $Bi_{12}TiO_{20}$) were detected. This proves that the dissolved titanium is consumed for the crystallization of $SrTiO_3$ and not for the formation of bismuth titanium compounds (e.g., $Bi_{12}TiO_{20}$). Single-phase $SrTiO_3$ was obtained after the dissolution of the side-products in 1 M HNO_3 (Figure 2 and Figure S2, Supporting information). A deeper insight into the process of the transformation from the initial $Bi_4Ti_3O_{12}$ platelets to $SrTiO_3$ was obtained by a microstructural investigation of the samples after the different times for the TC reaction. The partially and fully transformed platelets were examined by SEM and STEM from top and cross-sectional views. An SEM image of the powdered sample after 1 h of reaction is shown in Figure 3a. The initial morphology of the $Bi_4Ti_3O_{12}$ platelets is clearly preserved; however, the particles appear to have a core-rim structure. The XRD pattern of the platelets (cast from the isopropanol suspension of the platelets on the Si monocrystalline substrate) revealed the presence of $Bi_4Ti_3O_{12}$ and $SrTiO_3$ phases with preferential (001) and (100) orientations, respectively (Figure 2).

The sample after 1 h of transformation was investigated in more detail using the HAADF-STEM. A typical particle is shown in Figure 3b, and here, the core-rim structure is even more evident. In the dark-field (DF) image, the core of the particles is much brighter, indicating a higher atomic density in the core region, whereas the rim is more electron-transparent

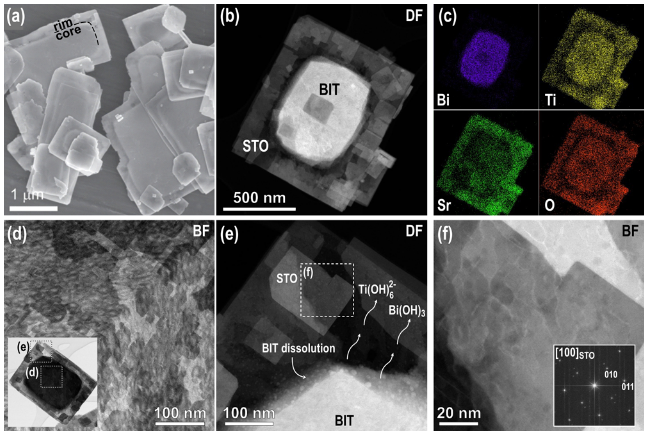

Figure 3. (a) SEM image of the heterostructural $SrTiO_3/Bi_4Ti_3O_{12}$ platelet with the core-rim structure after 1 h of the TC reaction at 200 °C (Sr/Ti = 12, 6 M NaOH). (b) STEM and (c) EDS analyses revealing the distribution of Bi, Ti, Sr, and O in the heterostructural platelet. (d) Close-up look with the focus set on the $SrTiO_3$ surface layer from the marked area of the platelet in the inset. (e) Magnified region around the core-rim contact showing the decomposition of $Bi_4Ti_3O_{12}$. (f) Higher magnification of the marked area in (e) and a fast Fourier transform (FFT) pattern in the inset.

due to the lower average atomic density or lesser thickness. More information about the chemical composition and the distribution of the elements in the particles were obtained from EDS mapping (Figure 3c) and EDS line profiles (Figure S4, Supporting Information). The results show that the core of the platelet is Bi-rich, whereas Sr is present everywhere with a higher amount in the rim. Signals from Ti and O were also detected in both parts of the platelets. The distribution of Sr all over the platelet indicates that the growth of $SrTiO_3$ occurs on the whole area of both basal surfaces, including both surface areas over the central part (core). According to the results of the STEM/EDS analyses, the core of the partially transformed $Bi_4Ti_3O_{12}$ platelets is mainly $Bi_4Ti_3O_{12}$, covered by $SrTiO_3$ on both sides, whereas the rim is newly formed $SrTiO_3$, which replaced $Bi_4Ti_3O_{12}$ in the dissolution−precipitation process. The platelet after 1 h of topochemical transformation can be regarded as a heterostructure of $Bi_4Ti_3O_{12}$ and $SrTiO_3$. Figure 3d (bright-field (BF) image) is a close-up of another partially transformed platelet in the middle region with the focus set on the surface layer. It shows the nucleation of nanosized crystallites, which occasionally show a rectangular morphology, as expected for the cubic $SrTiO_3$ structure. The presence of regions with distinctly different gray levels suggests that the crystallization of $SrTiO_3$ on the $Bi_4Ti_3O_{12}$ surface occurs in several layers and that the first layer is nanocrystalline, while

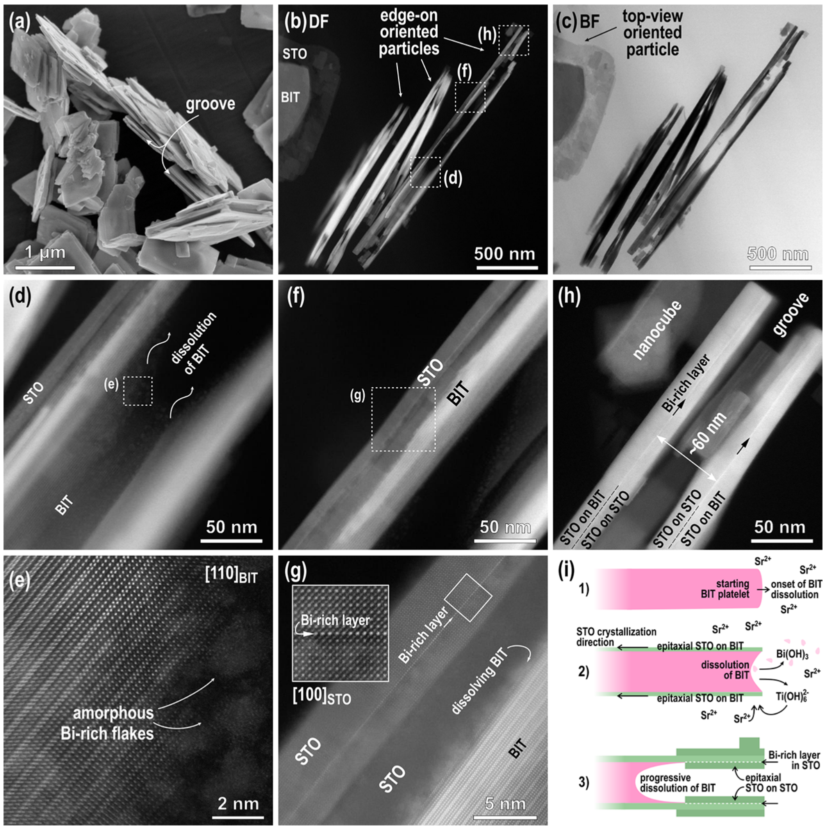

Figure 4. (a) SEM and (b−h) STEM micrographs of $SrTiO_3/Bi_4Ti_3O_{12}$ heterostructural platelets (mainly edge-on-oriented platelets, which were thinned to electron transparency) as obtained after 1 h of a reaction at 200 °C (6 M NaOH, Sr/Ti = 12). (b) DF and (c) BF images showing (mainly) edge-on platelets along the whole side length; (d) DF of the central part of the platelet (showing $SrTiO_3$ layers and partially disintegrated $Bi_4Ti_3O_{12}$ inside the groove). (e) HR image of the area marked in (d) showing the disintegration of $Bi_4Ti_3O_{12}$. (f) Another DF of the part between the central area and the edge of the platelet. (g) Magnified area from the image (f) presenting dissolution of $Bi_4Ti_3O_{12}$ and as-formed $SrTiO_3$ with the incorporated Bi-rich layer (HR image of this part is in the inset). (h) DF image of the edge of the platelet with two parallel $SrTiO_3$ platelets with incorporated Bi-rich layers. (i) Schematically shown processes of the TC reaction from $Bi_4Ti_3O_{12}$ to $SrTiO_3$ as reconstructed from STEM results, presented in (b)−(h).

https://dx.doi.org/10.1021/acsami.0c16253

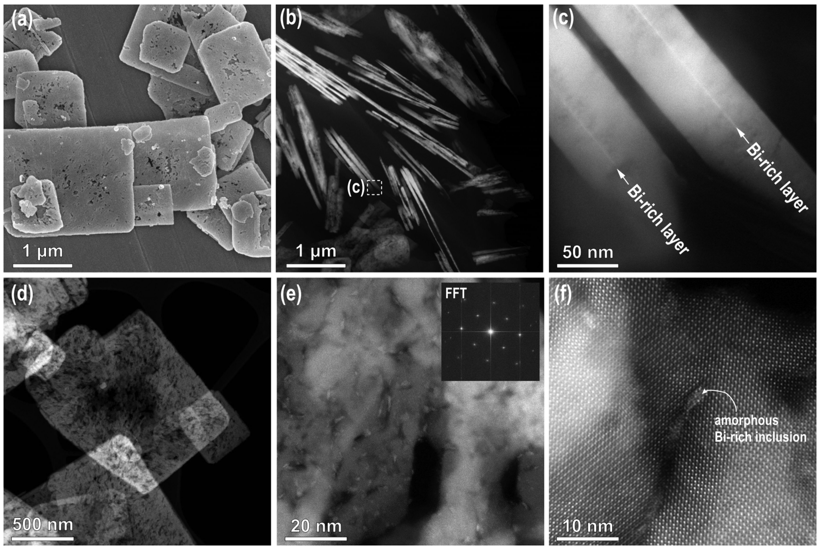

Figure 5. (a) SEM and (b−f) STEM DF images of (b, c) edge-on oriented $SrTiO_3$ platelets and (d−f) STEM top-view of $SrTiO_3$ platelets, formed after 15 h at 200 °C (Sr:Ti = 12, 6 M NaOH)). (e) STEM image from the central part with FFT showing a (100) orientation in the inset (f) HR image from the central part of the $SrTiO_3$ platelet with Bi-rich inclusion.

the crystallites in the upper layers are larger. This is also evident from Figure 3e,f where the fast Fourier transform (FFT) pattern of $SrTiO_3$ confirms the [100] orientation. Figure 3e also shows the borderline between the rim ($SrTiO_3$) and the core ($SrTiO_3/Bi_4Ti_3O_{12}/SrTiO_3$) where (during the hydrothermal reaction) $Bi_4Ti_3O_{12}$ disintegrates to $Ti(OH)_6^{2-}$ and $Bi(OH)_3$ (eq 2). The $Ti(OH)_6^{2-}$ ions, exsoluted from $Bi_4Ti_3O_{12}$, are consumed for the formation of $SrTiO_3$ according to eq 1, while $Bi(OH)_3$, through the condensation reactions, results in Bi_2O_3, as already confirmed by the XRD (Figure S3, Supporting information) and visible in the STEM as dots with bright contrast (Figure 3e). During the epitaxial crystallization of the $SrTiO_3$ nanodomains, some amorphous bismuth oxide-rich inclusions remain captured between the $SrTiO_3$ nanocrystallites.

An additional insight into the transformation process is obtained from the analysis of partially transformed heterostructure platelets in the edge-on orientation (Figure 4). An SEM image of the platelets in this orientation after 1 h of the TC reaction (200 °C, Sr/Ti = 12, 6 M NaOH) shows that a typical platelet contains a groove running along its edges, apparently splitting the platelet into two thinner parallel platelets (Figure 4a). A HAADF-STEM examination of the partially transformed platelets in an edge-on orientation reveals that the initial $Bi_4Ti_3O_{12}$ platelets actually start to separate into two parallel platelets aligned with the upper and lower basal-plane surfaces of the $Bi_4Ti_3O_{12}$ platelet. The process starts at the edges and proceeds toward the interior of the platelet (Figure 4b,c: DF−BF pair of STEM figures). One of the particles thinned to electron transparency almost along the whole area (cross-section) was investigated in more detail in three different regions—in the central part and toward the edge of the partially transformed platelet (Figure 4d−h). Figure 4d,e was taken in the central part where the particle has a sandwich structure composed of residual $Bi_4Ti_3O_{12}$ in the middle, which is surrounded by $SrTiO_3$ above and below the $Bi_4Ti_3O_{12}$. A closer look at the $Bi_4Ti_3O_{12}$ layer in this part of the platelet (Figure 4e) reveals that, here, the atomic layers of the $Bi_4Ti_3O_{12}$ structure, the $[Bi_2O_2]^{2+}$ sheets and the pseudo-perovskite $[Bi_2Ti_3O_{10}]^{2-}$ blocks, are subjected to intensive dissolution. The same process was already observed in the top-view (Figure 3e). $Bi_4Ti_3O_{12}$ disintegration is much faster from the lateral directions than from the top, as predicted on the basis of the difference of the basal and lateral surfaces with respect to the concentration of kink sites. Figure 4f,g were recorded in the region between the central part and the edge of the partially recrystallized $Bi_4Ti_3O_{12}$ particle. Here, the epitaxial orientation relationship between $SrTiO_3$ and $Bi_4Ti_3O_{12}$ in $[100]SrTiO_3\|[001]Bi_4Ti_3O_{12}$ is clearly visible and confirms that the orientation of $SrTiO_3$ is dictated by the structure of the underlying $Bi_4Ti_3O_{12}$ template. The fact that $SrTiO_3$ growth on the $Bi_4Ti_3O_{12}$ is epitaxial confirms that the reaction is TC.[13] In this part of the crystal, the $SrTiO_3$ layer was thinned to electron transparency (the $Bi_4Ti_3O_{12}$ part was completely etched away in some areas) and one of the most interesting features of the $SrTiO_3$ platelets that form during the TC transformation from $Bi_4Ti_3O_{12}$ under hydrothermal conditions is revealed, i.e., the presence of an atomic bismuth-rich layer (Bi-rich layer), inside the $SrTiO_3$ platelet (Figure 4g). Similarly, the STEM image of the platelet close to the edge (Figure 4h) in the section of complete transformation to $SrTiO_3$ (rim region in Figure 3) revealed the formation of two parallel $SrTiO_3$ platelets that both contain an atomic Bi-rich layer running along the middle part of both platelets. We believe that these Bi-rich layers correspond to the $[Bi_2O_2]^{2+}$-terminated top layers of the initial $Bi_4Ti_3O_{12}$ platelet.

The incorporation of the Bi-rich layer is also a consequence of the strong bonding between the termination layer of $Bi_4Ti_3O_{12}$ and growing $SrTiO_3$. Layer-by-layer growth (Frank−van der Merwe mechanism[38]), evident from our observations (Figure 3d), is also the result of strong bonding at the interface. The Bi-rich layer remains bonded to $SrTiO_3$ even after progressive dissolution of the remaining $Bi_4Ti_3O_{12}$ template. When the dissolution front of $Bi_4Ti_3O_{12}$ (inside the groove) reaches the Bi-rich layer, it remains attached to the epitaxial $SrTiO_3$ layer and the growth of the $SrTiO_3$ also proceeds from the inner side, and the Bi-rich layer becomes a coherent part of the newly formed $SrTiO_3$, where it is usually observed to be approximately in the middle of each $SrTiO_3$ platelet (Figure 4h). It is obvious that the formation of two

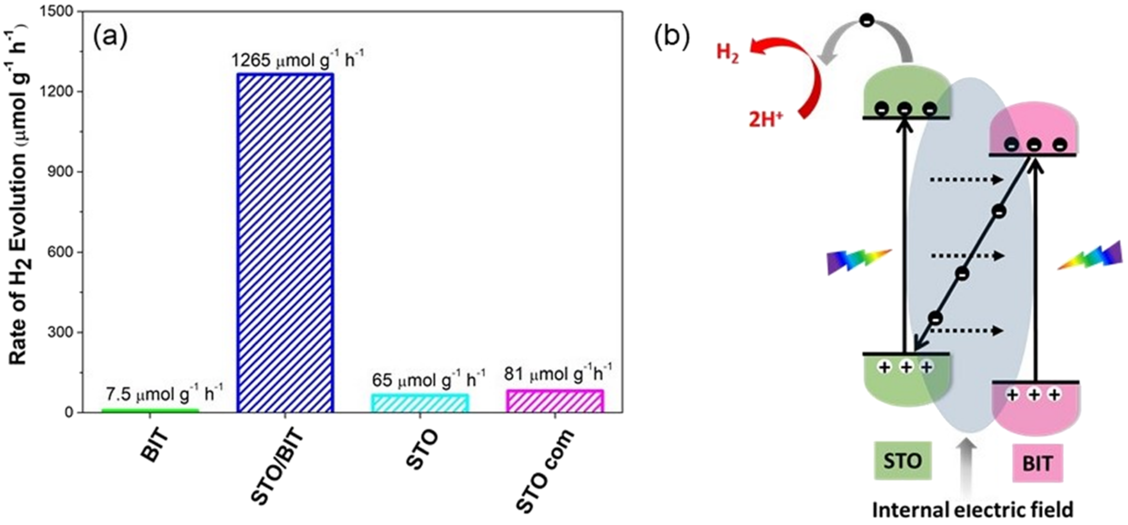

Figure 6. (a) Rate of H_2 evolution over the studied photocatalyst particles (20 mg) in 40 mL of aqueous solution with 25 vol % methanol without noble-metal cocatalysts. (b) Plausible photocatalytic H_2 evolution mechanism.

parallel platelets with an incorporated Bi-rich layer is the consequence of $SrTiO_3$ epitaxial growth on the both bismuth-oxide-terminated basal-plane surfaces of the $Bi_4Ti_3O_{12}$ platelets and continued $SrTiO_3$ growth on the inner side of the Bi-rich layers (Figure 4h).

It is clear from Figure 4h that the distance between the two Bi-rich layers, which actually represent a part of the $[Bi_2O_2]^{2+}$ terminating sheets on both sides of the starting $Bi_4Ti_3O_{12}$ platelet, is approximately 60 nm and corresponds to a typical thickness for starting $Bi_4Ti_3O_{12}$ template platelets (Figure 1). The attachment of $SrTiO_3$ nanocubes on both sides of the $SrTiO_3$ layers is also occasionally observed (Figure 4h). The conversion of $Bi_4Ti_3O_{12}$ to $SrTiO_3$, as reconstructed from investigations of edge-on-oriented, partially recrystallized platelets, is schematically shown in Figure 4i. The dissolution of the initial $Bi_4Ti_3O_{12}$ platelets starts from the lateral surfaces (Figure 4i, step 1) with a high concentration of atomic steps and where both types of structural units ($[Bi_2O_2]^{2+}$ sheets and the pseudo-perovskite $[Bi_2Ti_3O_{10}]^{2-}$ blocks) are exposed. The edging atoms are weakly bonded (Figure 1e). When the solution becomes locally saturated with Sr^{2+} and $Ti(OH)_6^{2-}$, nucleation of $SrTiO_3$ occurs in the areas with the lowest energy barrier. As noted earlier, the interfacial free energy for $SrTiO_3$ nucleation on the basal-plane surfaces of $Bi_4Ti_3O_{12}$ is low due to the close structural match at the interface and therefore, $SrTiO_3$ nucleation can immediately occur when saturation conditions are achieved. The areas close to the edges are subjected to higher concentrations of $Ti(OH)_6^{2-}$ from the beginning of the reaction, and therefore, $SrTiO_3$ nucleation starts there (Figure 4i, step 2). Then, with the progressive dissolution of the $Bi_4Ti_3O_{12}$, the growth of $SrTiO_3$ continues on both basal surfaces of the $Bi_4Ti_3O_{12}$ platelet. However, when the $Bi_4Ti_3O_{12}$ inside the groove completely dissolves to both the initially terminating Bi-rich layers, attached to the newly formed $SrTiO_3$, the epitaxial growth of $SrTiO_3$ also proceeds on the inner side of these Bi-rich layers and they become coherently integrated into the $SrTiO_3$ platelets on both sides. In the end, the Bi-rich layers lie approximately in the middle of each $SrTiO_3$ platelet half (Figure 4i, step 3; see also Figure 4h). The reactions of $Bi_4Ti_3O_{12}$ dissolution and $SrTiO_3$ precipitation (epitaxial growth) continue until there is complete dissolution of the $Bi_4Ti_3O_{12}$ matrix crystal. The $SrTiO_3$ platelets after 15 h of the reaction at 200 °C in 6 M NaOH and with a Sr:Ti ratio of 12 are shown in Figure 5. The general plate-like shape of the initial $Bi_4Ti_3O_{12}$ template particles is well preserved (Figure 5a); however, the integrity/crystallinity of the $SrTiO_3$ platelets reflects the specifics of the recrystallization mechanism. The final platelets usually consist of two intergrown $SrTiO_3$ platelets, as shown by the STEM analysis of the sample after 15 h of hydrothermal treatment (Figure 5b). The presence of $Bi_4Ti_3O_{12}$ between the $SrTiO_3$ platelets is not observed, indicating that all the $Bi_4Ti_3O_{12}$ molecules dissolved and $Ti(OH)_6^{2-}$was used for the formation of $SrTiO_3$. In the edge-on-oriented platelets, the two parallel Bi-rich atomic layers, which are a peculiarity of the studied hydrothermal TC reaction, were observed along the whole length of both $SrTiO_3$ platelet halves (Figure 5c).

From our calculation, a 60 nm-thin $Bi_4Ti_3O_{12}$ platelet would result in the formation of an approximately 42 nm-thin $SrTiO_3$ platelet (Figure S5, Supporting Information) or two parallel 21 nm-thin platelets; however, in the process of $Bi_4Ti_3O_{12}$ dissolution, the smallest $Bi_4Ti_3O_{12}$ crystallites most probably dissolve and then these $Ti(OH)_6^{2-}$ species are consumed for $SrTiO_3$ growth on the larger $Bi_4Ti_3O_{12}$ platelets. Therefore, the typical thickness of the final $SrTiO_3$ platelets is slightly larger and comparable to that of the initial $Bi_4Ti_3O_{12}$ platelets.

The crystallinity of the fully transformed $SrTiO_3$ platelets was analyzed in the top view (Figure 5d−f). A low-magnification STEM image of a thinner $SrTiO_3$ platelet is shown in Figure 5d. The crystal is relatively dense at the edges where the transformation starts, and the porosity of the platelet increases toward the central region of the platelet. A higher-magnification STEM image taken in the central part of the platelet with the FFT calculated from the whole area is shown in Figure 5e. It is clear that the matrix consists of epitaxially oriented nanocrystallites that formed (100)-oriented $SrTiO_3$ mesocrystalline platelets with some pores and nanosized inclusions with brighter contrast. The analysis showed that these are amorphous Bi-rich inclusions, which were trapped and overgrown by $SrTiO_3$ during the processes of $Bi_4Ti_3O_{12}$ dissolution and $SrTiO_3$ crystallization. The density of the amorphous Bi-rich inclusions appears to be higher in the central part of the $SrTiO_3$ platelets.

The observed morphological development resulted in an interesting variation of the BET specific surface area through the progress of the TC reaction. Actually, the measured BET values of the $SrTiO_3/Bi_4Ti_3O_{12}$ heterostructures increased in the first 6 h of the TC reaction, reaching a maximum at ~20 $m^2 \cdot g^{-1}$, and then the BET values decreased and approached that of $SrTiO_3$ (~10 $m^2 \cdot g^{-1}$), which was still higher than the BET value of the initial $Bi_4Ti_3O_{12}$ (2−3 $m^2 \cdot g^{-1}$) (Table S1, Supporting Information). The high specific surface area of the $SrTiO_3/Bi_4Ti_3O_{12}$ heterostructures is most probably related to the emerging groove and the high surface roughness of the growing $SrTiO_3$ layers. Smoothening of the surface of the $SrTiO_3$ platelets with the completion of the TC reaction is the reason for the lower specific surface area of the final $SrTiO_3$ platelets compared to that of the heterostructures.

3.4. Photocatalytic Performance. To demonstrate the potential of the developed $Bi_4Ti_3O_{12}$, $SrTiO_3/Bi_4Ti_3O_{12}$ and mesocrystalline $SrTiO_3$ platelets, the as-prepared materials were tested and assessed in terms of the photocatalytic activity for H_2 evolution in pH-neutral aqueous media (H_2O/CH_3OH = 75/25). The results were compared to those involving commercial $SrTiO_3$ nanopowders that were evaluated under the same conditions (Figure 6a). The $Bi_4Ti_3O_{12}$ platelets with the smallest specific surface area, approximately 2−3 $m^2 \cdot g^{-1}$ (Supporting Information, Table S1), were found to exhibit the lowest H_2 evolution rate among the studied materials, only 7.5 $\mu mol \cdot g^{-1} \cdot h^{-1}$. Mesocrystalline (100)-oriented $SrTiO_3$ platelets (65 $\mu mol \cdot g^{-1} \cdot h^{-1}$) and commercial nanocrystalline $SrTiO_3$ powders (81 $\mu mol \cdot g^{-1} \cdot h^{-1}$) show comparable photocatalytic activities, although the specific surface area of the platelets (10 $m^2 \cdot g^{-1}$) was lower than that of the commercial nanopowder (24 $m^2 \cdot g^{-1}$). An extraordinarily higher H_2 evolution rate (1265 $\mu mol \cdot g^{-1} \cdot h^{-1}$) was observed for the heterostructural $SrTiO_3/Bi_4Ti_3O_{12}$ platelets (Figure 6a and Table S1, Supporting Information). In this study, the enhanced photocatalytic performance for H_2 evolution is only presented for the heterostructural $SrTiO_3/Bi_4Ti_3O_{12}$ platelets with a $SrTiO_3/Bi_4Ti_3O_{12}$ weight ratio of 60/40 and BET = 20 $m^2 \cdot g^{-1}$ (Figure S6, Supporting information). We confirmed several times that the heterostructural platelets exhibiting a BET surface area of >15 $m^2 \cdot g^{-1}$ typically show a considerably higher H_2 evolution rate than the pure $SrTiO_3$ platelets and the commercial $SrTiO_3$ nanopowders. The results support the important role of the heterojunction for an improvement of the photocatalytic efficiency. A systematic study of the mutual effect of the $SrTiO_3/Bi_4Ti_3O_{12}$ ratio and the specific surface area on the photocatalytic H_2 evolution is beyond the scope of the present article, and the results of this research will be published in a forthcoming study. It is noteworthy that the relatively high H_2 evolution rate was determined for bare nanoheterostructural $SrTiO_3/Bi_4Ti_3O_{12}$ platelets without any noble-metal doping or cocatalyst support. In terms of the H_2 production rate, our heterostructures demonstrate better performance than several other noble-metal-loaded photocatalysts (Table S2, Supporting Information).[19−22,39−41] Cycled measurements of the H_2 evolution revealed good repeatability and reusability of the nanoheterostructural $SrTiO_3/Bi_4Ti_3O_{12}$ platelets (Figure 6 and Figure S7). The stability of the H_2 evolution over the tested 24 h reaction time is similar to that reported for other $SrTiO_3$-based photocatalysts (Figure S7).[23,24]

A band-structure analysis is an essential approach to provide a deep insight into the possible photocatalytic mechanism. The band-gap energy (E_g) of the constituents was calculated using the well-known Tauc method from the UV−vis diffuse reflectance spectra and Kubelka−Munk function (see calculation in the Supporting Information and Figure S8).[42] The obtained band gaps for $SrTiO_3$ and $Bi_4Ti_3O_{12}$ were 3.23 and 3.16 eV, respectively. The conduction band (E_{CB}) and valence band (E_{VB}) energies, another two important factors, are calculated using the empirical formulas (see calculation in the Supporting Information).[43−45] The E_{CB} and E_{VB} of $SrTiO_3$ were determined to be −0.80 and 2.43 eV, while for $Bi_4Ti_3O_{12}$, the calculations revealed an E_{CB} = −0.21 eV and E_{VB} = 2.95 eV. For $SrTiO_3$, the calculated E_{CB} (−0.8 eV) perfectly matches the reported E_{CB} value (−0.81 eV[7,17]), determined by the Mott−Schottky method for single-crystalline $SrTiO_3$.[17] In contrast, in the case of $Bi_4Ti_3O_{12}$, a larger deviation was observed between the calculated E_{CB} (−0.21 eV) and those E_{CB} values obtained from the Mott−Schottky plot (−0.1 eV[46] and −0.41 eV[47]). The discrepancies are not unexpected since these experimental values were determined for two different $Bi_4Ti_3O_{12}$ nanostructures.[46,47] Namely, it is known that the experimental determination of the fundamental characteristics (e.g., E_{CB}) of nanostructural materials is associated with a high degree of uncertainty.[48] This is also true for the determination of E_{CB} from the Mott−Schottky relationship, which is based on several assumptions and ideal conditions, which are not entirely fulfilled by nanostructures.[48,49]

Finally, another important parameter, the Fermi energy (E_F), is determined according to the estimation that it lies at 0.3−0.1 eV below E_{CB} for n-type semiconductors. These values are −0.51 and −0.11 eV for $SrTiO_3$ and $Bi_4Ti_3O_{12}$, respectively (Figure S9, Supporting Information), and also support the previous results.[50,51] The studied heterostructural $SrTiO_3/Bi_4Ti_3O_{12}$ platelets can be categorized as staggered type II alignments, and for this current research, we found that the potential of water reduction (at pH 7) lies in between $E_{CB}/SrTiO_3$ and $E_{CB}/Bi_4Ti_3O_{12}$.[5] Figure S8c (Supporting Information) shows the modified band gap of the heterojunction, and this supports the band rearrangements as well. Under simulated-light irradiation, the constituent elements absorb photons, and as a result, electron/hole pairs are generated (Figure 6b). It is already determined that $E_F/SrTiO_3$ lies in a more negative position than $E_F/Bi_4Ti_3O_{12}$. During Fermi-level rearrangement, due to the higher Fermi energy of $SrTiO_3$, the electrons tend to move from $SrTiO_3$ to $Bi_4Ti_3O_{12}$. This phenomenon causes the $SrTiO_3$ and $Bi_4Ti_3O_{12}$ sites to be positively and negatively charged, respectively. As a result, a weak internal electric field is generated at the solid−solid interface. Therefore, the photo-generated electrons prefer to migrate from a CB of $Bi_4Ti_3O_{12}$ to a VB of $SrTiO_3$ via this low-resistance pathway. This prevents the electron/hole recombination, and this study supports the possible execution of a Z-scheme transfer (Figure 6b).[52,53] For this experiment, the coupling of $SrTiO_3$ and $Bi_4Ti_3O_{12}$ greatly facilitates the photo-generated carrier transfer and separation of electron/hole pairs under light irradiation and, as a result, the H_2 evolution rate is enhanced significantly. Here, the holes at $VB/Bi_4Ti_3O_{12}$ were consumed by the hole-scavenger methanol.[54] PL spectroscopy with an excitation wavelength of 320 nm was used to evaluate the separation efficiencies of the photo-excited charge carriers in the studied photocatalyst platelets (Figure 7). The $Bi_4Ti_3O_{12}$ platelets show strong PL emission peaks at approximately 415 and 450 nm, which is in line with the reported PL spectra of $Bi_4Ti_3O_{12}$.[25,47] As compared to pure $Bi_4Ti_3O_{12}$, the $SrTiO_3/Bi_4Ti_3O_{12}$ heterostructures show a significantly lower PL

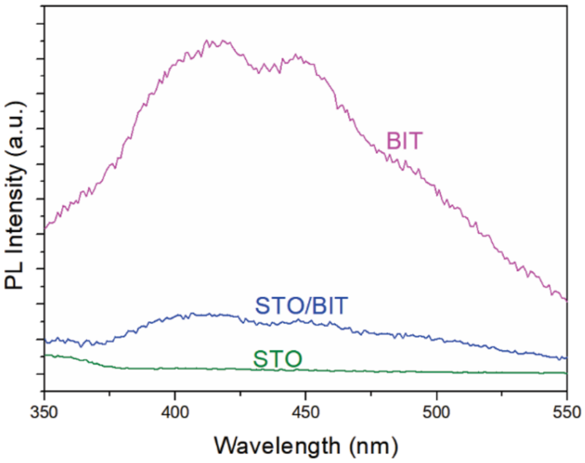

Figure 7. Photoluminescence (PL) spectra of the $Bi_4Ti_3O_{12}$, $SrTiO_3/Bi_4Ti_3O_{12}$ heterostructure ($SrTiO_3/Bi_4Ti_3O_{12}$ = 60/40), and $SrTiO_3$ platelets.

intensity. This result suggests the inhibition of charge recombination in the $SrTiO_3/Bi_4Ti_3O_{12}$ heterostructure, resulting in an improvement of its photocatalytic activity. In contrast to $Bi_4Ti_3O_{12}$, the $SrTiO_3$ platelets do not show a significant visible PL, which is typical for non-defective $SrTiO_3$.[18,55]

In terms of band-gap energy, the $SrTiO_3/Bi_4Ti_3O_{12}$ heterostructural platelets are, similar to $SrTiO_3$, UV-active photocatalysts. Due to the small portion of UV light in the incident light spectra, the $SrTiO_3$-based photocatalysts do not show a high solar-to-hydrogen (STH) efficiency. It has been reported that a modification of the $SrTiO_3$ by doping and/or cocatalyst deposition led to a variation of the STH from 0.037 to 0.65% (Table S3, Supporting Information).[22,24,56−59] The highest STH efficiency (0.65%) was reported by Domen and co-workers[24] for Al-doped $SrTiO_3$ loaded with Rh/Cr_2O_3 and CoOOH cocatalysts. An STH greater than 1% was demonstrated for La- and Rh-codoped $SrTiO_3$ (H_2 evolution) combined with Mo-doped $BiVO_4$ (O_2 evolution) and Au in the Z-scheme-based photocatalysts.[56] In the current study, $SrTiO_3/Bi_4Ti_3O_{12}$ heterostructural platelets without any noble-metal doping or cocatalyst loading exhibit an STH efficiency of 0.19%, which is moderate but comparable to several other reported STH values for noble-metal decorated $SrTiO_3$ photocatalysts (Table S3, Supporting Information). Considering that the $SrTiO_3/Bi_4Ti_3O_{12}$ heterostructure was evaluated for the first time in terms of photocatalytic H_2 evolution, we believe that there is still room for improvement in its STH efficiency.

4. CONCLUSIONS

The epitaxial growth of $SrTiO_3$ on $Bi_4Ti_3O_{12}$ template platelets was studied under alkaline hydrothermal conditions at 200 °C to illustrate the TC reaction for the formation of novel $SrTiO_3/Bi_4Ti_3O_{12}$ heterostructural platelets and (100)-oriented $SrTiO_3$ mesocrystalline platelets. In the presented TC reaction, the $Bi_4Ti_3O_{12}$ platelets act as a source of dissolved $Ti(OH)_6^{2-}$ species and also serve as a substrate for epitaxial growth of $SrTiO_3$. The heterogeneously layered structure of the $Bi_4Ti_3O_{12}$ platelets with different dissolution rates of the basal and lateral surfaces results in an interesting morphological development and additionally offers a unique track and insight into the hydrothermal TC mechanism. Dissolution of the initial $Bi_4Ti_3O_{12}$ platelet from the lateral ends into the interior and the simultaneous epitaxial growth of $SrTiO_3$ on both bismuth-oxide-terminated basal-surface planes of the template platelet result in the formation of two parallel $SrTiO_3$ platelets separated by a groove that deepens with the progress of the TC reaction, whereas $Bi_4Ti_3O_{12}$ constitutes the core of the $SrTiO_3/Bi_4Ti_3O_{12}$ heterostructural platelet. When the TC reaction is completed, the newly formed platelet-like particle consists of two parallel $SrTiO_3$ platelets, both of which have an incorporated monoatomic Bi-rich layer, the remains of the top layers of the parent $Bi_4Ti_3O_{12}$ platelet.

The intermediate heterostructural $SrTiO_3/Bi_4Ti_3O_{12}$ and the final $SrTiO_3$ platelets develop approximately 5−10 times higher specific surfaces (10−20 $m^2 \cdot g^{-1}$) than the initial $Bi_4Ti_3O_{12}$ platelets, mainly due to the newly formed groove and the high surface roughness of the growing $SrTiO_3$. The photocatalytic activity for the H_2 evolution and the STH efficiency of the as-prepared $SrTiO_3/Bi_4Ti_3O_{12}$ platelets free of noble-metal cocatalysts are reproducible, stable, and 18 times (1265 $\mu mol \cdot g^{-1} \cdot h^{-1}$; STH = 0.19%) higher than that of the (100)-oriented $SrTiO_3$ mesocrystalline platelets (65 $\mu mol \cdot g^{-1} \cdot h^{-1}$; STH = 0.01%) and 15 times more than that of the commercial $SrTiO_3$ nanopowders (81 $\mu mol \cdot g^{-1} \cdot h^{-1}$; STH = 0.012%). The enhanced photocatalytic activity of the $SrTiO_3/Bi_4Ti_3O_{12}$ heterostructural platelets is explained by the efficient transfer of the photogenerated carriers from $Bi_4Ti_3O_{12}$ to $SrTiO_3$ and separation of electron/hole pairs at the interface. The reduced recombination of photoinduced charge carriers in the $SrTiO_3/Bi_4Ti_3O_{12}$ heterostructural platelets was confirmed by the decreased intensity of the photoluminescence.

The detailed insight into the mechanism of epitaxial growth for $SrTiO_3$ on $Bi_4Ti_3O_{12}$ expands the possibilities for using the hydrothermal TC reaction concept in the design of highly preferentially oriented heterostructures or mesocrystallites, involving other template particles and growing phases for the preparation of new efficient photocatalyst systems.

■ ASSOCIATED CONTENT

Supporting Information

The Supporting Information is available free of charge at https://pubs.acs.org/doi/10.1021/acsami.0c16253.

Electron microscopy analyses, XRD patterns, photocatalytic data, and the calculation of the band structures (PDF)

■ AUTHOR INFORMATION

Corresponding Author

Marjeta Maček Kržmanc − *Advanced Materials Department, Jožef Stefan Institute, 1000 Ljubljana, Slovenia;* orcid.org/0000-0003-3436-5692; Phone: +386 1 477 3292; Email: marjeta.macek@ijs.si

Authors

Nina Daneu − *Advanced Materials Department, Jožef Stefan Institute, 1000 Ljubljana, Slovenia*
Alja Čontala − *Advanced Materials Department, Jožef Stefan Institute, 1000 Ljubljana, Slovenia; Jožef Stefan International Postgraduate School, 1000 Ljubljana, Slovenia*
Saswati Santra − *Advanced Materials Department, Jožef Stefan Institute, 1000 Ljubljana, Slovenia;* orcid.org/0000-0003-0327-0279

Khaja Mohaideen Kamal − *Department of Catalysis and Chemical Reaction Engineering, National Institute of Chemistry, 1000 Ljubljana, Slovenia*
Blaž Likozar − *Department of Catalysis and Chemical Reaction Engineering, National Institute of Chemistry, 1000 Ljubljana, Slovenia;* orcid.org/0000-0001-7226-4302
Matjaž Spreitzer − *Advanced Materials Department, Jožef Stefan Institute, 1000 Ljubljana, Slovenia*

Complete contact information is available at:
https://pubs.acs.org/10.1021/acsami.0c16253

Notes

The authors declare no competing financial interest.

■ ACKNOWLEDGMENTS

The authors acknowledge the M-era.Net projects (HarvEnPiez (no. 3184), contract no. C3330-17-500075, and SunToChem (no. 6081), contract no. C3330-19-252011), project no. J1-9177 and research program no. P2-0091, which were financially supported by the Ministry of Higher Education, Science and Technology and the Slovenian Research Agency, respectively. A.Č. is grateful to the Slovenian Research Agency for the financial support of her PhD study (no. PR-07596). The authors would also like to thank to Katarina Lapornik, Dominika Zorman, Tina Pečarič, and Špela Kaps for their help in the synthesis of the samples, Medeja Gec for the preparation of the samples for the TEM examinations, and Dr. Špela Kunej for performing the UV−vis spectroscopic measurements.

■ REFERENCES

(1) Xiong, Z.; Kuang, C. C.; Lin, K. Y.; Lei, Z.; Chen, X.; Gong, B.; Yang, J.; Zhao, Y.; Zhang, J.; Xia, B.; Wu, J. C. S. Enhanced CO_2 Photocatalytic Reduction through Simultaneously Accelerated H_2 Evolution and CO_2 Hydrogenation in a Twin Photoreactor. *J. CO2 Util.* **2018**, *24*, 500−508.

(2) Mu, L.; Zhao, Y.; Li, A.; Wang, S.; Wang, Z.; Yang, J.; Wang, Y.; Liu, T.; Chen, R.; Zhu, J.; Fan, F.; Li, R.; Li, C. Enhancing Charge Separation on High Symmetry $SrTiO_3$ Exposed with Anisotropic Facets for Photocatalytic Water Splitting. *Energy Environ. Sci.* **2016**, *9*, 2463−2469.

(3) Afroz, K.; Moniruddin, M.; Bakranov, N.; Kudaibergenov, S.; Nuraje, N. A Heterojunction Strategy to Improve the Visible Light Sensitive Water Splitting Performance of Photocatalytic Materials. *J. Mater. Chem. A* **2018**, *6*, 21696−21718.

(4) Li, D.; Yu, J. C.-C.; Nguyen, V. H.; Wu, J. C. S.; Wang, X. A Dual-Function Photocatalytic System for Simultaneous Separating Hydrogen from Water Splitting and Photocatalytic Degradation of Phenol in a Twin-Reactor. *Appl. Catal., B* **2018**, *239*, 268−279.

(5) Chen, S.; Takata, T.; Domen, K. Particulate Photocatalysts for Overall Water Splitting. *Nat. Rev. Mater.* **2017**, *2*, 17050.

(6) Li, X.; Yu, J.; Jaroniec, M. Hierarchical Photocatalysts. *Chem. Soc. Rev.* **2016**, *45*, 2603−2636.

(7) Zhang, P.; Ochi, T.; Fujitsuka, M.; Kobori, Y.; Majima, T.; Tachikawa, T. Topotactic Epitaxy of $SrTiO_3$ Mesocrystal Superstructures with Anisotropic Construction for Efficient Overall Water Splitting. *Angew. Chem., Int. Ed. Engl.* **2017**, *56*, 5299−5303.

(8) Guo, E.; Yin, L. Tailored $SrTiO_3/TiO_2$ Heterostructures for Dye-Sensitized Solar Cells with Enhanced Photoelectric Conversion Performance. *J. Mater. Chem. A* **2015**, *3*, 13390−13401.

(9) Poterala, S. F.; Chang, Y.; Clark, T.; Meyer, R. J., Jr.; Messing, G. L. Mechanistic Interpretation of the Aurivillius to Perovskite Topochemical Microcrystal Conversion Process. *Chem. Mater.* **2010**, *22*, 2061−2068.

(10) Chang, Y.; Ning, H.; Wu, J.; Zhang, S.; Lü, T.; Yang, B.; Cao, W. Formation Mechanism of (001) Oriented Perovskite $SrTiO_3$ Microplatelets Synthesized by Topochemical Microcrystal Conversion. *Inorg. Chem.* **2014**, *53*, 11060−11067.

(11) Kržmanc, M. M.; Uršič, H.; Meden, A.; Korošec, R. C.; Suvorov, D. $Ba_{1-x}Sr_xTiO_3$ Plates: Synthesis through Topochemical Conversion, Piezoelectric and Ferroelectric Characteristics. *Ceram. Int.* **2018**, *44*, 21406−21414.

(12) Kržmanc, M. M.; Jančar, B.; Uršič, H.; Tramšek, M.; Suvorov, D. Tailoring the Shape, Size, Crystal Structure, and Preferential Growth Orientation of $BaTiO_3$ Plates Synthesized through a Topochemical Conversion Process. *Cryst. Growth Des.* **2017**, *17*, 3210−3220.

(13) Kalyani, V.; Vasile, B. S.; Ianculescu, A.; Testino, A.; Carino, A.; Buscaglia, M. T.; Buscaglia, V.; Nanni, P. Hydrothermal Synthesis of $SrTiO_3$: Role of Interfaces. *Cryst. Growth Des.* **2015**, *15*, 5712−5725.

(14) Kalyani, V.; Vasile, B. S.; Ianculescu, A.; Buscaglia, M. T.; Buscaglia, V.; Nanni, P. Hydrothermal Synthesis of $SrTiO_3$ Mesocrystals: Single Crystal to Mesocrystal Transformation Induced by Topochemical Reactions. *Cryst. Growth Des.* **2012**, *12*, 4450−4456.

(15) Canu, G.; Buscaglia, V. Hydrothermal Synthesis of Strontium Titanate: Thermodynamic Considerations, Morphology Control and Crystallisation Mechanisms. *CrystEngComm* **2017**, *19*, 3867−3891.

(16) Zhang, Y.; Chen, Z.; Lu, Z. A Facile Method for the Preparation of Colored $Bi_4Ti_3O_{12-x}$ Nanosheets with Enhanced Visible-Light Photocatalytic Hydrogen Evolution Activity. *Nanomaterials* **2018**, *8*, 261.

(17) Bolts, J. M.; Wrighton, M. S. Correlation of Photocurrent-Voltage Curves with Flat-Band Potential for Stable Photoelectrodes for the Photoelectrolysis of Water. *J. Phys. Chem.* **1976**, *80*, 2641−2645.

(18) Zhou, X.; Liu, N.; Yokosawa, T.; Osvet, A.; Miehlich, M. E.; Meyer, K.; Spiecker, E.; Schmuki, P. Intrinsically Activated $SrTiO_3$: Photocatalytic H_2 Evolution from Neutral Aqueous Methanol Solution in the Absence of Any Noble Metal Cocatalyst. *ACS Appl. Mater. Interfaces* **2018**, *10*, 29532−29542.

(19) Zhao, Z.; Willard, E. J.; Li, H.; Wu, Z.; Castro, R. H. R.; Osterloh, F. E. Aluminum Enhances Photochemical Charge Separation in Strontium Titanate Nanocrystal Photocatalysts for Overall Water Splitting. *J. Mater. Chem. A* **2018**, *6*, 16170−16176.

(20) Kuang, Q.; Yang, S. Template Synthesis of Single-Crystal-Like Porous $SrTiO_3$ Nanocube Assemblies and Their Enhanced Photocatalytic Hydrogen Evolution. *ACS Appl. Mater. Interfaces* **2013**, *5*, 3683−3690.

(21) Puangpetch, T.; Sreethawong, T.; Yoshikawa, S.; Chavadej, S. Hydrogen Production from Photocatalytic Water Splitting over Mesoporous-Assembled $SrTiO_3$ Nanocrystal-Based Photocatalysts. *J. Mol. Catal. A: Chem.* **2009**, *312*, 97−106.

(22) Wang, Q.; Hisatomi, T.; Ma, S. S. K.; Li, Y.; Domen, K. Core/Shell Structured La- and Rh-Codoped $SrTiO_3$ as a Hydrogen Evolution Photocatalyst in Z-Scheme Overall Water Splitting under Visible Light Irradiation. *Chem. Mater.* **2014**, *26*, 4144−4150.

(23) Chiang, T. H.; Lyu, H.; Hisatomi, T.; Goto, Y.; Takata, T.; Katayama, M.; Minegishi, T.; Domen, K. Efficient Photocatalytic Water Splitting Using Al-Doped $SrTiO_3$ Coloaded with Molybdenum Oxide and Rhodium−Chromium Oxide. *ACS Catal.* **2018**, *8*, 2782−2788.

(24) Takata, T.; Jiang, J.; Sakata, Y.; Nakabayashi, M.; Shibata, N.; Nandal, V.; Seki, K.; Hisatomi, T.; Domen, K. Photocatalytic Water Splitting with a Quantum Efficiency of Almost Unity. *Nature* **2020**, *581*, 411−414.

(25) Chen, Z.; Jiang, X.; Zhu, C.; Shi, C. Chromium-Modified $Bi_4Ti_3O_{12}$ Photocatalyst: Application for Hydrogen Evolution and Pollutant Degradation. *Appl. Catal., B* **2016**, *199*, 241−251.

(26) Hou, J.; Cao, R.; Wang, Z.; Jiao, S.; Zhu, H. Chromium-Doped Bismuth Titanate Nanosheets as Enhanced Visible-Light Photocatalysts with a High Percentage of Reactive {110} Facets. *J. Mater. Chem.* **2011**, *21*, 7296−7301.

(27) Zhang, H.; Chen, G.; Li, X. Synthesis and Visible Light Photocatalysis Water Splitting Property of Chromium-Doped $Bi_4Ti_3O_{12}$. *Solid State Ionics* **2009**, *180*, 1599−1603.

(28) Wu, J.; Chang, Y.; Lv, W.; Jiang, G.; Sun, Y.; Liu, Y.; Zhang, S.; Yang, B.; Cao, W. Topochemical Transformation of Single Crystalline $SrTiO_3$ Microplatelets from $Bi_4Ti_3O_{12}$ Precursors and their Orientation-Dependent Surface Piezoelectricity. *CrystEngComm* **2018**, *20*, 3084−3095.

(29) Zhao, W.; Wang, H.; Feng, X.; Jiang, W.; Zhao, D.; Li, J. Hydrothermal Synthesis and Photocatalytic Activities of $Bi_4Ti_3O_{12}$/$SrTiO_3$ Composite Micro-Platelets. *Mater. Res. Bull.* **2015**, *70*, 179−183.

(30) Čontala, A.; Maček Kržmanc, M.; Suvorov, D. Plate-Like $Bi_4Ti_3O_{12}$ Particles and their Topochemical Conversion to $SrTiO_3$ Under Hydrothermal Conditions. *Acta Chim. Slov.* **2018**, *65*, 630−637.

(31) Snyder, R. C.; Doherty, M. F. Faceted Crystal Shape Evolution During Dissolution or Growth. *AIChE J.* **2007**, *53*, 1337−1348.

(32) Lencka, M. M.; Riman, R. E. Thermodynamics of the Hydrothermal Synthesis of Calcium Titanate with Reference to Other Alkaline-Earth Titanates. *Chem. Mater.* **1995**, *7*, 18−25.

(33) Livage, J.; Henry, M.; Sanchez, C. Sol-Gel Chemistry of Transition Metal Oxides. *Prog. Solid State Chem.* **1988**, *18*, 259−341.

(34) Li, L.; Fijneman, A. J.; Kaandorp, J. A.; Aizenberg, J.; Noorduin, W. L. Directed Nucleation and Growth by Balancing Local Supersaturation and Substrate/Nucleus Lattice Mismatch. *Proc. Natl. Acad. Sci. U. S. A.* **2018**, *115*, 3575−3580.

(35) Maxim, F.; Ferreira, P.; Vilarinho, P. M.; Reaney, I. Hydrothermal Synthesis and Crystal Growth Studies of $BaTiO_3$ Using Ti Nanotube Precursors. *Cryst. Growth Des.* **2008**, *8*, 3309−3315.

(36) Maxim, F.; Vilarinho, P. M.; Ferreira, P.; Reaney, I. M.; Levin, I. Kinetic Study of the Static Hydrothermal Synthesis of $BaTiO_3$ Using Titanate Nanotubes Precursors. *Cryst. Growth Des.* **2011**, *11*, 3358−3365.

(37) Bartonickova, E.; Cihlar, J.; Castkova, K. Microwave-Assisted Synthesis of Bismuth Oxide. *Process. Appl. Ceram.* **2007**, *1*, 29−33.

(38) Markov, I. V. *Crystal Growth for Beginners Fundamentals of Nucleation, Crystal Growth and Epitaxy*; 2nd Editio.; World Scientific: Singapore, 2003. DOI: 10.1142/5172.

(39) Huang, B.-S.; Wey, M.-Y. Properties and H_2 Production Ability of Pt Photodeposited on the Anatase Phase Transition of Nitrogen-Doped Titanium Dioxide. *Int. J. Hydrogen Energy* **2011**, *36*, 9479−9486.

(40) Wu, Z.-L.; Wang, C.-H.; Zhao, B.; Dong, J.; Lu, F.; Wang, W.-H.; Wang, W.-C.; Wu, G.–J.; Cui, J.-Z.; Cheng, P. A Semi-Conductive Copper-Organic Framework with Two Types of Photocatalytic Activity. *Angew. Chem., Int. Ed.* **2016**, *55*, 4938−4942.

(41) Zhang, G.; Lan, Z.-A.; Lin, L.; Lin, S.; Wang, X. Overall Water Splitting by Pt/g-C_3N_4 Photocatalysts without Using Sacrificial Agents. *Chem. Sci.* **2016**, *7*, 3062−3066.

(42) Makuła, P.; Pacia, M.; Macyk, W. How To Correctly Determine the Band Gap Energy of Modified Semiconductor Photocatalysts Based on UV-Vis Spectra. *J. Phys. Chem. Lett.* **2018**, *9*, 6814−6817.

(43) Lin, X. P.; Huang, F. Q.; Wang, W. D.; Zhang, K. L. A Novel Photocatalyst $BiSbO_4$ for Degradation of Methylene Blue. *Appl. Catal., A* **2006**, *307*, 257−262.

(44) Mousavi, M.; Habibi-Yangjeh, A.; Abitorabi, M. Fabrication of Novel Magnetically Separable Nanocomposites Using Graphitic Carbon Nitride, Silver Phosphate and Silver Chloride and Their Applications in Photocatalytic Removal of Different Pollutants Using Visible-Light Irradiation. *J. Colloid Interface Sci.* **2016**, *480*, 218−231.

(45) Cao, T.; Li, Y.; Wang, C.; Zhang, Z.; Zhang, M.; Shao, C.; Liu, Y. $Bi_4Ti_3O_{12}$ Nanosheets/TiO_2 Submicron Fibers Heterostructures: *In Situ* Fabrication and High Visible Light Photocatalytic Activity. *J. Mater. Chem.* **2011**, *21*, 6922−6927.

(46) Zhao, X.; Yang, H.; Li, S.; Cui, Z.; Zhang, C. Synthesis and Theoretical Study of Large-Sized $Bi_4Ti_3O_{12}$ Square Nanosheets with High Photocatalytic Activity. *Mater. Res. Bull.* **2018**, *107*, 180−188.

(47) Liu, Y.; Zhu, G.; Gao, J. Z.; Hojamberdiev, M.; Lu, H.; Zhu, R.; Wei, X.; Liu, P. A Novel CeO_2/$Bi_4Ti_3O_{12}$ Composite Heterojunction Structure with an Enhanced Photocatalytic Activity for Bisphenol A. *J. Alloys Compd.* **2016**, *688*, 487−496.

(48) Hankin, A.; Bedoya-Lora, F. E.; Alexander, J. C.; Regoutz, A.; Kelsall, G. H. Flat Band Potential Determination: Avoiding the Pitfalls. *J. Mater. Chem. A* **2019**, *7*, 26162−26176.

(49) Cardon, F.; Gomes, W. P. On the Determination of the Flat-Band Potential of a Semiconductor in Contact with a Metal or an Electrolyte from the Mott-Schottky Plot. *J. Phys. D: Appl. Phys.* **1978**, *11*, L63.

(50) Schafranek, R.; Li, S.; Chen, F.; Wu, W.; Klein, A. $PbTiO_3$/$SrTiO_3$ Interface: Energy Band Alignment and its Relation to the Limits of Fermi Level Variation. *Phys. Rev. B: Condens. Matter Mater. Phys.* **2011**, *84*, No. 045317.

(51) Al-Keisy, A.; Ren, L.; Xu, X.; Hao, W.; Dou, S. X.; Du, Y. Selective Ferroelectric BiOI/$Bi_4Ti_3O_{12}$ Heterostructures for Visible Light-Driven Photocatalysis. *J. Phys. Chem. C* **2019**, *123*, 517−525.

(52) Ng, B.-J.; Putri, L. K.; Kong, X. Y.; Teh, Y. W.; Pasbakhsh, P.; Chai, S.-P. Z-Scheme Photocatalytic Systems for Solar Water Splitting. *Adv. Sci.* **2020**, 1903171.

(53) Yu, W.; Xu, D.; Peng, T. Enhanced Photocatalytic Activity of g-C_3N_4 for Selective CO_2 Reduction to CH_3OH *via* Facile Coupling of ZnO:A Direct Z-scheme Mechanism. *J. Mater. Chem. A* **2015**, *3*, 19936−19947.

(54) Denisov, N.; Yoo, J. E.; Schmuki, P. Effect of Different Hole Scavengers on the Photoelectrochemical Properties and Photocatalytic Hydrogen Evolution Performance of Pristine and Pt-Decorated TiO_2 Nanotubes. *Electrochim. Acta* **2019**, *319*, 61−71.

(55) Kan, D.; Terashima, T.; Kanda, R.; Masuno, A.; Tanaka, K.; Chu, S.; Kan, H.; Ishizumi, A.; Kanemitsu, Y.; Shimakawa, Y.; Takano, M. Blue-Light Emission at Room Temperature from Ar^+-Irradiated $SrTiO_3$. *Nat. Mater.* **2005**, *4*, 816−819.

(56) Wang, Q.; Hisatomi, T.; Jia, Q.; Tokudome, H.; Zhong, M.; Wang, C.; Pan, Z.; Takata, T.; Nakabayashi, M.; Shibata, N.; Li, Y.; Sharp, I. D.; Kudo, A.; Yamada, T.; Domen, K. Scalable Water Splitting on Particulate Photocatalyst Sheets with a Solar-to-Hydrogen Energy Conversion Efficiency Exceeding 1%. *Nat. Mater.* **2016**, *15*, 611−615.

(57) Goto, Y.; Hisatomi, T.; Wang, Q.; Higashi, T.; Ishikiriyama, K.; Maeda, T.; Sakata, Y.; Okunaka, S.; Tokudome, H.; Katayama, M.; Akiyama, S.; Nishiyama, H.; Inoue, Y.; Takewaki, T.; Setoyama, T.; Minegishi, T.; Takata, T.; Yamada, T.; Domen, K. A Particulate Photocatalyst Water-Splitting Panel for Large-Scale Solar Hydrogen Generation. *Joule* **2018**, *2*, 509−520.

(58) Zhao, Z.; Goncalves, R. V.; Barman, S. K.; Willard, E. J.; Byle, E.; Perry, R.; Wu, Z.; Huda, M. N.; Moulé, A. J.; Osterloh, F. E. Electronic Structure Basis for Enhanced Overall Water Splitting Photocatalysis with Aluminum Doped $SrTiO_3$ in Natural Sunlight. *Energy Environ. Sci.* **2019**, *12*, 1385−1395.

(59) Lyu, H.; Hisatomi, T.; Goto, Y.; Yoshida, M.; Higashi, T.; Katayama, M.; Takata, T.; Minegishi, T.; Nishiyama, H.; Yamada, T.; Sakata, Y.; Asakura, K.; Domen, K. An Al-doped $SrTiO_3$ Photocatalyst Maintaining Sunlight-Driven Overall Water Splitting Activity for Over 1000 h of Constant Illumination. *Chem. Sci.* **2019**, *10*, 3196−3201.